Science Advances

AAAS

Supplementary Materials for

Programmable droplet manipulation by a magnetic-actuated robot

An Li, Huizeng Li*, Zheng Li, Zhipeng Zhao, Kaixuan Li, Mingzhu Li, Yanlin Song*

*Corresponding author. Email: ylsong@iccas.ac.cn (Y.S.); lhz1990@iccas.ac.cn (H.L.)

The PDF file includes:

Other Supplementary Material for this manuscript includes the following:

Section S1. Mechanical analysis of the droplet behaviors manipulated by the magnetic-actuated robot

To have a deep understanding of the droplet behaviors, we systematically analyzed the forces in the droplet manipulating processes, and divided the droplet evolution into two stages.

The first stage is the movement of the front three-phase contact line (TCL) between the two beads, as shown by the blue dotted line in Figure 1. The moving of the beads induces the deformation of the droplet due to the liquid-solid adhesion force. If the front TCL cannot move with the beads, the droplet will be released. Otherwise, the droplet transport or split will occur. There are three forces influencing the first stage: the driving force is the adhesion force between the beads and the droplet (F_a), and the resisting forces are the elastic force due to the droplet deformation (F_e) and the adhesion force between the substrate and the front TCL (f_{front}). As shown in Figure 1, the driving force F_a is expressed as

$$F_a = \oint \gamma \cos \delta \, (\pi d \cdot \sin \frac{\beta}{2}) \mathrm{d}l \qquad (1)$$

where γ is the liquid surface tension, d is the diameter of the beads, δ is the angle between the tangent line of TCL and the moving direction, β is the central angle between the contact points of the TCL and the bead, l is the contour of the TCL around the bead.
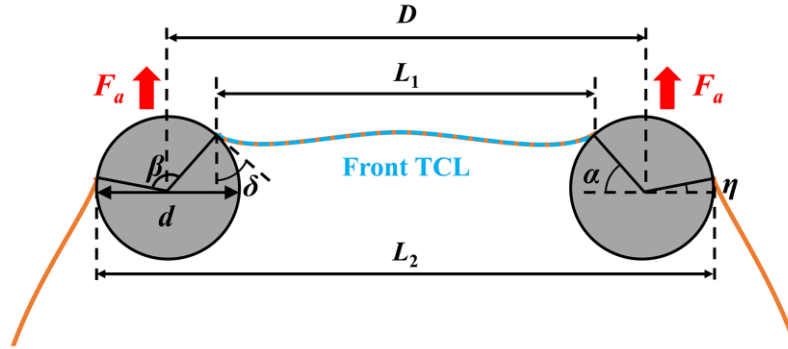

Figure 1. Illustration of the front TCL and parameters describing the droplet in the first stage.

We hypothesize that the droplet obeys the Hooke's law within a certain deformation range. Considering the droplet as a spring, one of the resisting forces, the elastic force (F_e) originates from the deformation of the droplet, can be expressed as

$$F_e = E \cdot \varepsilon \cdot A \qquad (2)$$

where E is the elastic modulus of the droplet, ε is the ratio of the droplet stretched length to the maximum stretched length ($\varepsilon = y/y_{max}$, as shown in Figure 2A), A is the cross-section area of the droplet behind the front TCL (Figure 2B). To simplify the calculation, the cross-section is considered to be rectangular, so its area is expressed as $A \approx d \cdot D$.
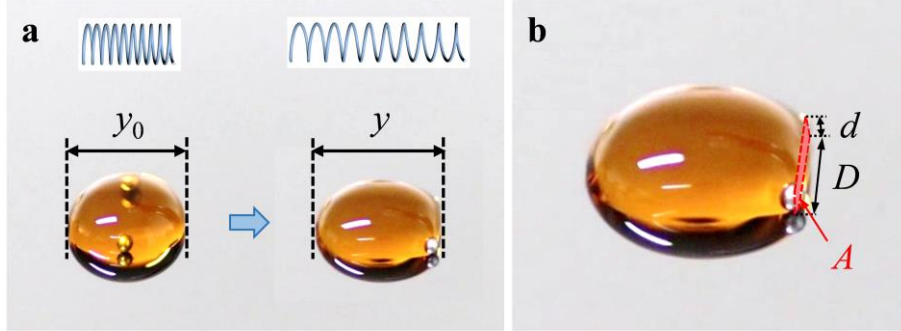

Figure 2. Display of the droplet evolution and the illustration of the parameters in the first stage.

The other resisting force is the adhesion force on the front TCL (f_{front})

$$f_{front} = \gamma \cos \theta_{adv} \cdot L_1 \qquad (3)$$

where θ_{adv} is the advancing contact angle of the droplet on the substrate, L_1 is the width of the front TCL, and $L_1 = D - d \cos\alpha$ (Figure 1). It is noteworthy that f_{front} is negative in the moving direction.

Therefore, the net force at the front end of the droplet is

$$F_{front} = 2F_a - F_e - f_{front} = 2 \oint \gamma \cos \delta \left(\pi d \cdot \sin \frac{\beta}{2} \right) dl - E \cdot \varepsilon \cdot A + \gamma \cos \theta_{adv} \cdot L_1 \qquad (4)$$

If the resisting force cannot be overcome by the driving force ($F_{front} \leq 0$), the front TCL will be pinned, making the droplet released by the robot. Otherwise ($F_{front} > 0$), the front TCL is pulled by the robot and the droplet split or transport will occur, depending on the force balancing at the rear end.

The second stage is the movement of the droplet rear end, which is determined by the rear TCL. As shown in Figure 3A, the rear TCL refers to the rest part except the front TCL (the blue dotted

line). In this stage, the driving force is the elastic force (F_e), and the resisting force is the adhesion force on the rear TCL (f_{rear}).

The elastic force (F_e) generates from the stretched droplet, which is equal to the elastic force in the first stage.

The rear TCL is divided into three parts: Ψ_1, Ψ_2 and Ψ_3 (Figure 3B). The adhesion force on the rear TCL is

$$f_{rear} = f_{rear1} + f_{rear2} + f_{rear3} \qquad (5)$$

The adhesion force on Ψ_1 is

$$f_{rear1} = \gamma \cdot L_2 \cdot \cos\theta_{rec} \qquad (6)$$

where θ_{rec} is the receding contact angles of the liquid on the substrate, L_2 is the width of the liquid between the beads, and $L_2 = D + d\cos\eta$, L_3 is the maximum width of the three-phase contact line contour between the droplet and the substrate (Figure 3A).

The adhesion forces on Ψ_2 and Ψ_3 are

$$f_{rear2} = f_{rear3} = \gamma \cdot (L_3 - L_2)(\cos\theta_{rec} - \cos\theta_{adv})/2 \qquad (7)$$

The net force on the rear end (F_{rear}) is

$$F_{rear} = F_e - f_{rear} = E \cdot \varepsilon \cdot A - \gamma(\cos\theta_{rec} - \cos\theta_{adv})L_3 - \cos\theta_{adv} \cdot L_2 \qquad (8)$$

The droplet can be transported if $F_{rear} > 0$, otherwise a daughter-drop will be split from the original droplet.
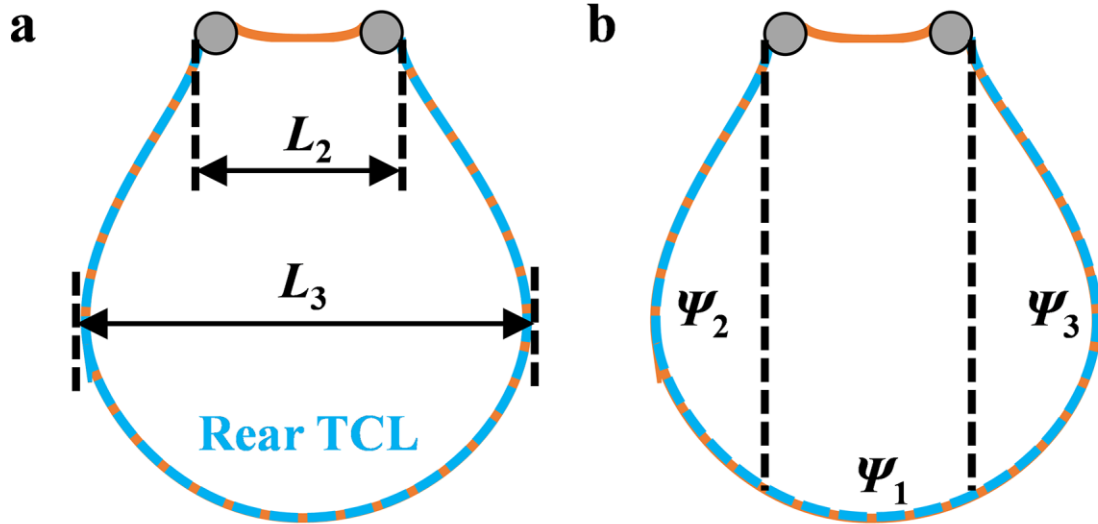
Figure 3. Illustration of the rear TCL and its three constituent parts.

Section S2. Detailed analysis of the phase diagram
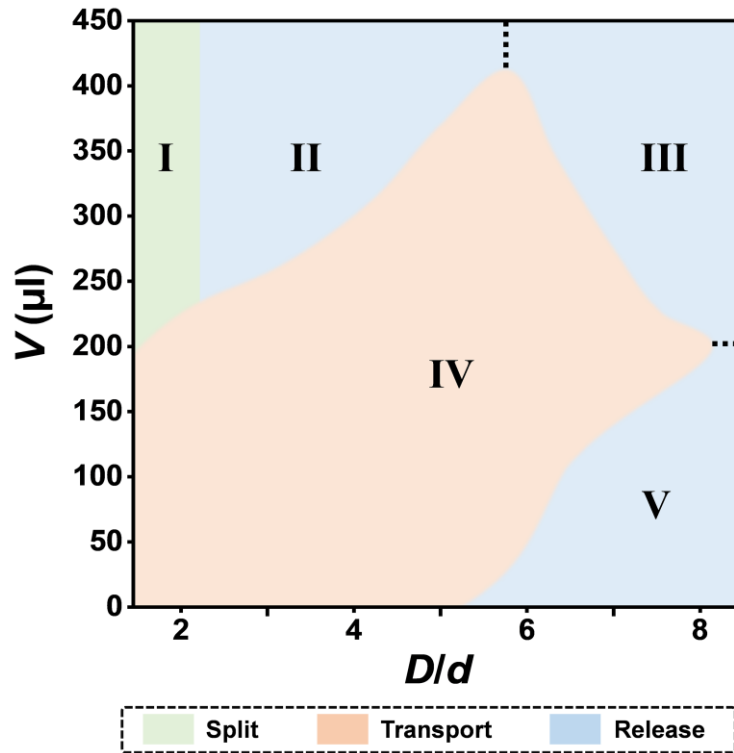
Figure 4. Illustration of the five regions in the phase diagram.

To have a deep understanding of the droplet behaviors transitions, we divide the phase diagram into five regions as shown in Figure 4. The region I represents the droplet split, the region IV represents the droplet transport. The region of droplet release is divided into three regions (II, III and V) because of the different occurrence mechanism.

Figure 5. Demonstration of typical droplet evolutions in the region I and the region II.

In our experiments, the diameter of the beads (d) is fixed at 1.2 mm, and we discuss the effect of the beads distance (D), on behalf of D/d, on the droplet manipulation behaviors. Firstly, we discuss the transition from split to release (from the region I to the region II), which is realized by enlarging D. Figure 5 shows the typical evolution of the droplet shapes during split and release. Note that the front TCL moves and the rear TCL is pinned in the droplet s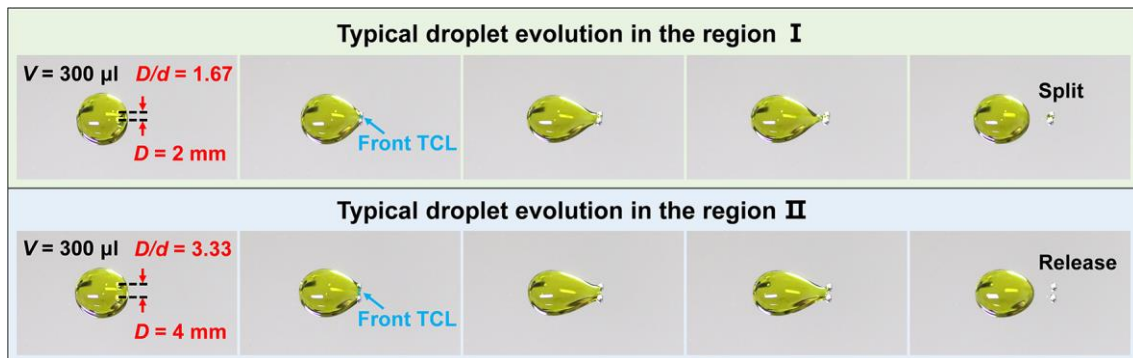plit (the region I), while both the front and rear TCLs are pinned in the droplet release (the region II). According to the mechanical analysis in Text S1, the movement of the front TCL is governed by the driving force and the resisting forces. When the droplet is split by the robot, the driving force F_a is larger than the total resisting force ($F_e + f_{front}$).

According to Equation 3, f_{front} increases with the increasing of D. In accordance with the mechanism analysis in Text S1

$$F_e = E \cdot \varepsilon \cdot A = E \cdot \varepsilon \cdot d \cdot D \qquad (9)$$

Therefore, an increase in D leads to an increase in F_e. When D increases to the critical value, the total resisting force ($F_e + f_{front}$) becomes greater than the driving force (F_a) and the front TCL is pinned. As a result, the droplet is released by the robot.
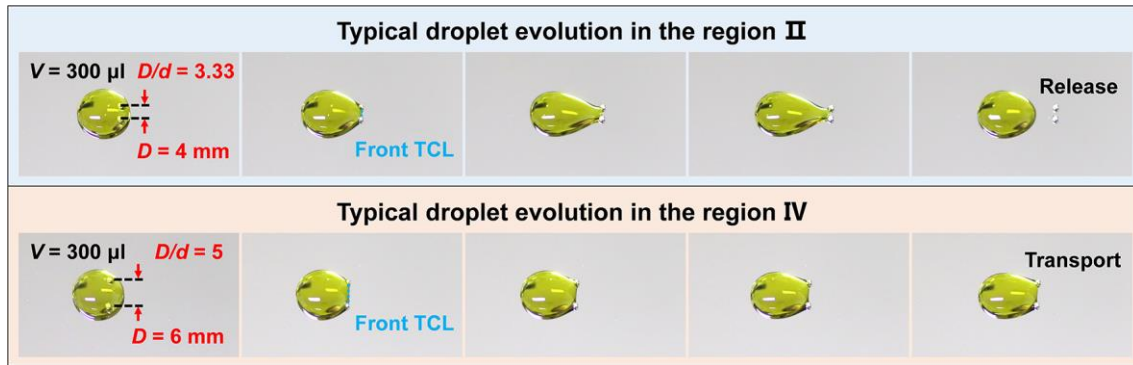
Figure 6. Demonstration of typical droplet evolution in the region II and the region IV.

Then we discuss the effect of D on the transition of the droplet behaviors from release to transport (from the regions II to IV) with a fixed droplet volume (Figure 6). When the droplet is released by the robot, the front and rear TCLs are pinned (the region II), while the moving of the front and rear TCLs induces droplet transport.

The rear TCL is mainly governed by the resisting force f_{rear}

$$f_{\text{rear}} = \gamma(\cos\theta_{\text{rec}} - \cos\theta_{\text{adv}})L_3 + \gamma\cos\theta_{\text{adv}}L_2 \qquad (10)$$

Note that L_2 is positively related with D: $L_2 = D + d\cos\eta$. On the basis of Equation (10), f_{rear} decreases with the increasing of L_2 because $\cos\theta_{\text{adv}} < 0$. So it is much easier to move the rear TCL by increasing D. Meanwhile, the increasing of D enlarges the driving force F_a, making the front TCL move (Figure 1 and Equation 1).
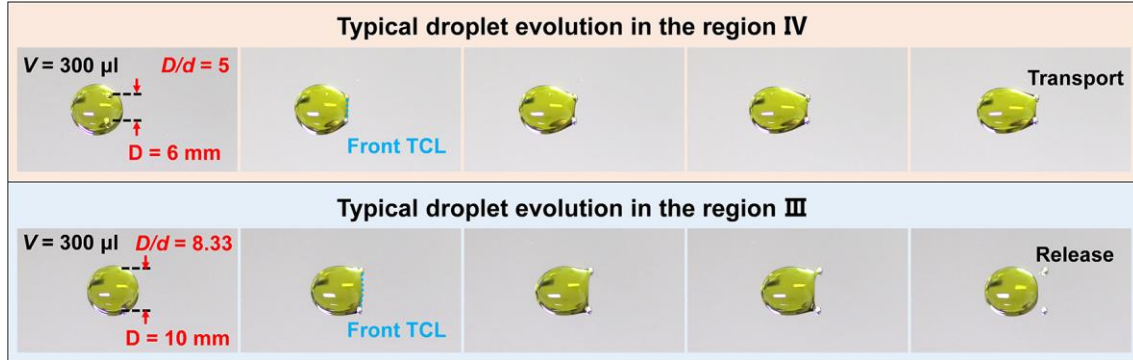

Figure 7. Demonstration of typical droplet evolution in the region IV and the region III.

As shown in Figure 7, the increasing D results in the transition of droplet behaviors from transport to release (from the region IV to III), which is regulated by the adhesion force at the front TCL (f_{front}). According to Equation 3 and the relationship of $L_1 = D - d\cos\alpha$, a large D generates a large f_{front}. When D is larger than a critical value, the front TCL will be pinned on the substrate. As a result, the droplet will not greatly deform, but produce two liquid bridges behind the beads. Subsequently, the liquid bridges break and the droplet release occurs.

Figure 8. Demonstration of typical droplet evolution in the region V.

In Figure 8, we demonstrate the evolution of the droplet behavior in the area V. In this part, the droplet is longitudinal stretched due to the small volume and the large D. An elastic force F_e', vertical to the moving direction, exists even the beads do not move. When the beads start to move, the droplet undergoes lateral stretching in addition to longitudinal stretching, which results in a large F_e on the front TCL. Meanwhile, there is a large f_{front} due to the large beads distance D

in the region V. As a result, the resisting force, consisting of F_e and f_{front}, exceeds the maximum value of F_a, and the droplet is released by the robot.

However, the extent of the longitudinal stretching of the droplet decreases as the volume of the droplets increases, and F_e on the front TCL is reduced. So the droplets with a larger volume can be transport by the robot (from the region V to the region IV).

Section S3. Analysis of factors affecting droplet manipulation behaviors

For the droplet manipulation behaviors such as split, transport and release, the control principle can be summarized as:

Table R1. Control principle of different droplet manipulation behaviors.

	Manipulation behaviors		
	Transport	Split	Release
Movement of the front TCL	Yes	Yes	No
Movement of the rear TCL	Yes	No	No

Generally, to realize the droplet transport, we need to move both the front and rear TCLs; to realize the droplet splitting, the front TCL is dragged to move, while the rear TCL remains fixed; to realize the droplet release, both the front and rear TCLs should keep fixed. Many factors influence the droplet manipulation behaviors, which affect the movement of the front and rear TCLs, as elaborated below:

1. Effect of the substrate advancing and receding contact angles

As explained in the manuscript, the droplet manipulation is realized by the movements of TCLs at the front and rear ends of the droplet, which are greatly affected by the advancing and receding contact angles. We performed droplet manipulation tests on various substrates with different advancing and receding contact angles. The manipulation results are summarized in Table R2. It can be concluded that in our tests, the largest advancing and smallest receding contact angles that can realize multiple manipulations are 121° (achieved on the PFCTS-Si) and 13 ° (achieved on the untreated glass), respectively.

Moreover, we added a droplet manipulation phase diagrams in Figure 9, which is performed on an APTES-Si plate with the advancing and receding contact angles of 90° and 59°, respectively.

By comparison, the advancing and receding contact angles of the substrate used for the phase diagram in our manuscript are 115° and 86°, respectively. We can find that the phase diagram in Figure 9 shows great difference from the phase diagram in Fig. 2A in our manuscript.
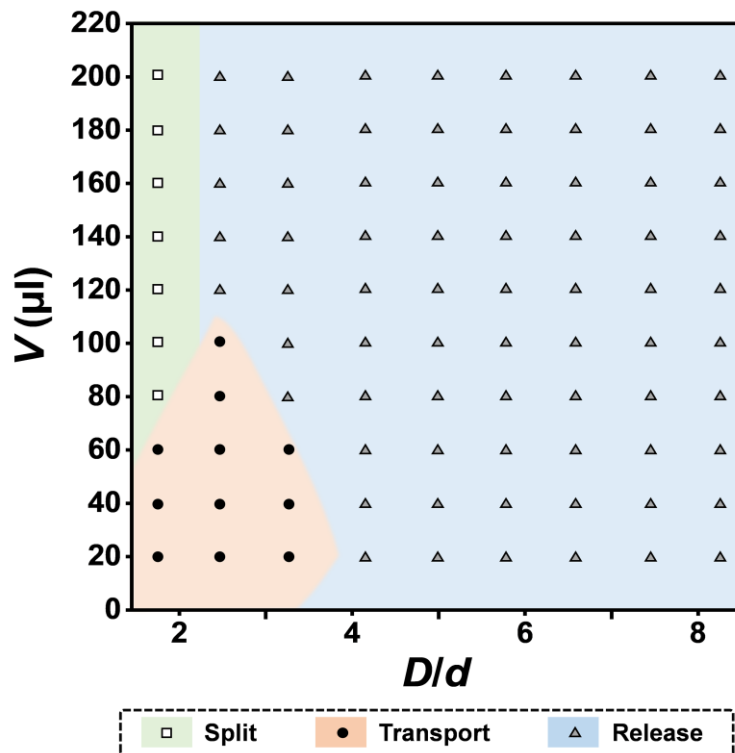

Figure 9. Phase diagram to show the droplet manipulation abilities with the variation of *D/d* and *V*.

Table R2. Droplet manipulation on substrates with different advancing and receding contact angles.

Sample	θ_{adv} (°)	θ_{rec} (°)	Transport	Split	Release	Rotation
APTES-Glass	86	52	√	√	√	√
APTES-Al	135	<5	×	×	×	√
APTES-Si	90	59	√	√	√	√
MPTMS-Glass	82	36	√	√	√	√
MPTMS-Al	129	6	×	×	√	√
MPTMS-Si	84	48	√	√	√	√
PFCTS-Glass	114	70	√	√	√	√
PFCTS-Si	121	88	√	√	√	√
PFOTS-Glass	112	77	√	√	√	√
PFOTS-Al	140	127	√	×	×	√
PFOTS-Si	115	86	√	√	√	√
PE	93	57	√	√	√	√

PTFE	96	50	√	√	√	√
Untreated Glass	49	13	√	√	√	√
Untreated Si	62	32	√	√	√	√

Notes: APTES: 3-aminopropyltriethoxysilane; Al: porous anodized aluminum sheet; Si: silicon wafer, MPTMS: (3-mercaptopropyl)trimethoxysilane; PFCTS: 1H, 1H, 2H, 2H-perfluorooctyltrichlorosilane; PFOTS: 1H, 1H, 2H, 2H-perfluorodecyltrimethoxysilane. The term "A-B" means that B is modified by A. For example, "APTES-Glass" means that the glass substrate is modified by the reagent of 3-Aminopropyltriethoxysilane.

2. Effect of the droplet surface tension

On the one hand, the surface tension determines the curvature of the droplet sitting on the substrate, which affect the advancing and receding contact angles of the droplet. On the other hand, the surface tension affects the driving forces at both the front and rear ends of the droplet. Enlarge the droplet surface tension increases both of the driving forces, which contributes to the movement of the front and rear TCLs. And the maximum volume of droplets that can be transport by the robot increases as the increases of the droplet surface tension.

3. Effect of the beads moving speed

An increase in the velocity of the droplet leads to an increase in the resistance of the droplet movement. The movement of the front TCL and the rear TCL are both affected. According the mechanical analysis in S1, the maximum volume of droplets that can be transport by the robot decrease as the increase of the beads moving speed. We product experiments to investigate the influence of the magnetic-actuated robot moving speed and the liquid surface tension on the droplet manipulation behaviors, and the results are displayed in Figure 10. *D/d* of these tests is fixed at 3.33. The moving speed in Figure 10B is fixed as 2 mm/s.
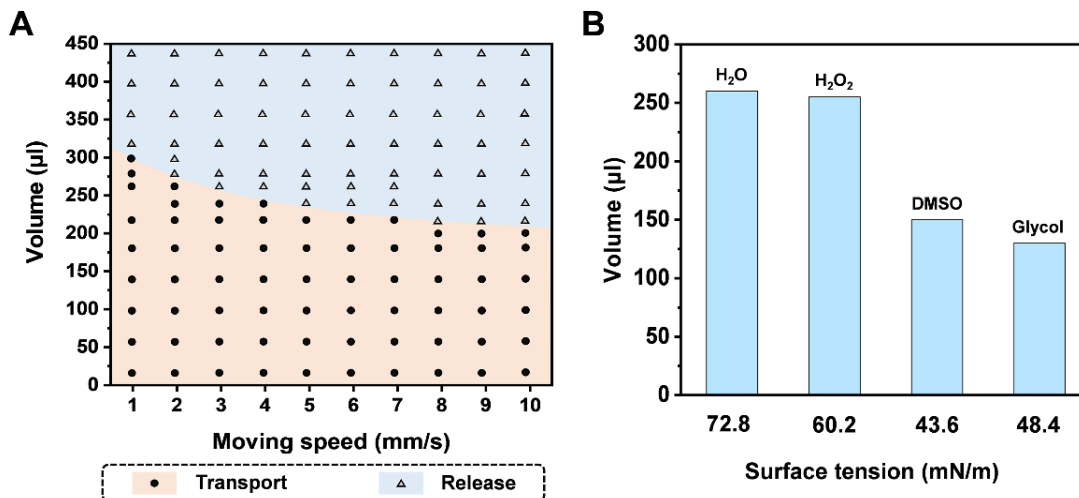
Figure 10. Influence of the magnetic-actuated robot moving speed and the liquid surface tension on the droplet manipulation behaviors.

4. Effect of the bead surface wettability

The droplet movement is actuated by the fraction (or adhesion) between the beads and the droplet, which is decided by the morphology of the beads. Normally, the fraction (or adhesion) should be large enough to capture the droplet and conduct the follow-up manipulation behaviors. Enhance the hydrophilicity of the beads will enlarge the fraction in a certain range.

5. Effect of the beads size

The size of the steel beads also has influence on the droplet manipulation processes. We performed a series of tests with different beads sizes to illustrate the relationship between the beads size and the droplet manipulation function, as summarized in the phase diagrams below (Figure 11). In the four phase diagrams, the beads distances (D) are fixed at 2 mm, 4 mm, 6 mm, and 8 mm, respectively. For each of the phase diagram, the beads diameters are 0.4 mm, 0.6 mm, 0.8 mm, 1.0 mm, 1.2 mm, 1.5 mm, and 2.0 mm, respectively. For all the phase diagrams, enlarging the bead size contributes to the droplet manipulation change from release to transportation. This can be explained that the driving power increases with the enlarging of the bead size (d), as indicated by equation (4).
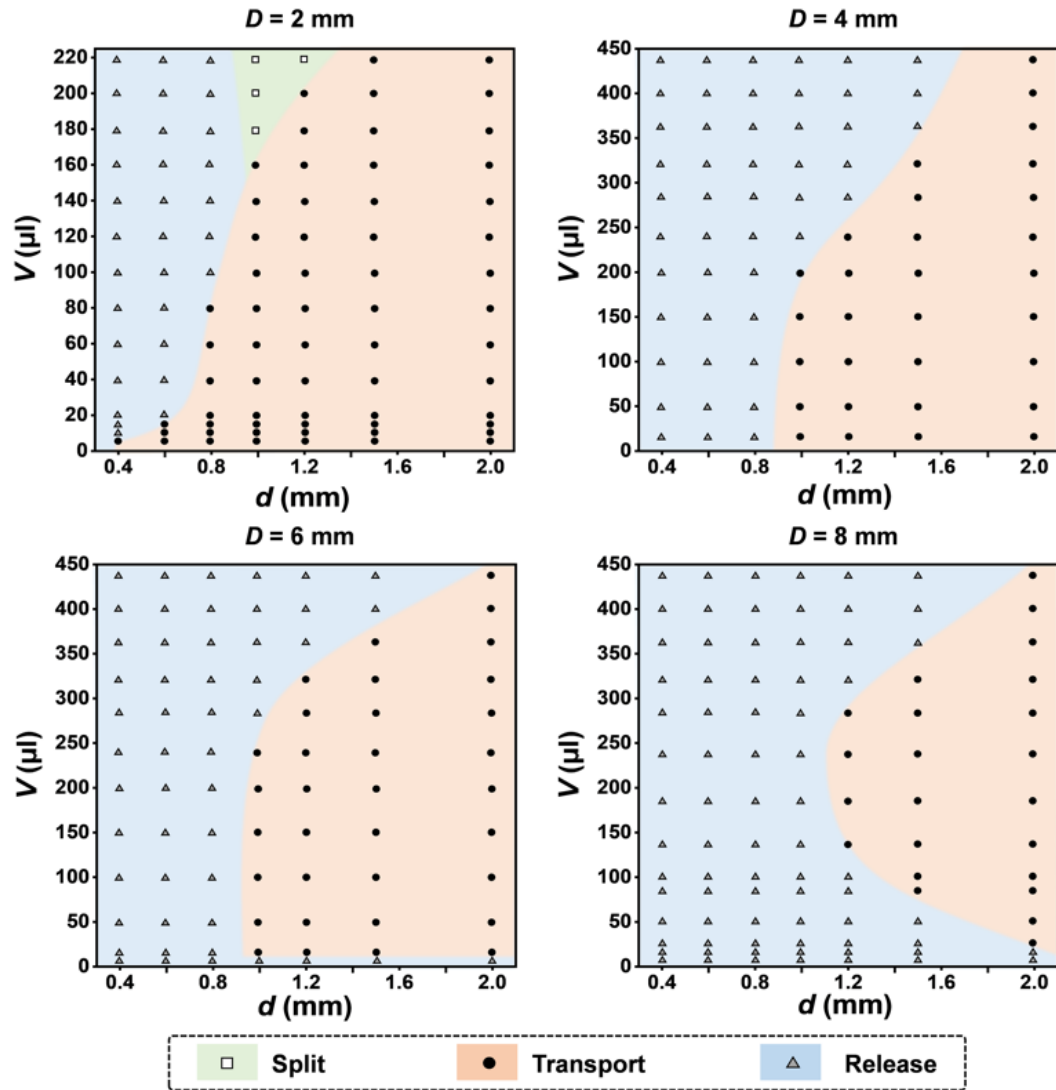
Figure 11. Dependence of the droplet manipulation functions on the bead size (*d*) at different beads distances (*D*).

Section S4. Principle of the bead surface modification

In the manuscript, we used superhydrophobic, superhydrophilic and unmodified beads for different manipulation environments. For example, we manipulate gas bubbles under water using superhydrophobic beads, manipulate water droplets under oil using superhydrophilic beads. The key principle is that the contact between the beads and the manipulated fluid (fluid-2) cannot be replaced by the contact between the beads and the bulk fluid (fluid-1). This can be presented that the Gibbs energy change during the replace process should be positive

$$\Delta G = \gamma_{1,s} - \gamma_{2,s} > 0 \tag{11}$$

where $\gamma_{1,s}$ is the interface energy between the fluid-1 and the bead, $\gamma_{2,s}$ is the interface energy between the fluid-2 and the bead. According to the Young's equation, the force balance on the three-phase contact line can be expressed as

$$\gamma_{1,s} = \gamma_{2,s} + \gamma_{1,2} cos\alpha \tag{12}$$

where α is the contact angle. So, we can obtain the quantitative criterion for the effective surface modification

$$cos\alpha = \frac{\gamma_{1,s} - \gamma_{2,s}}{\gamma_{1,2}} = \frac{\Delta G}{\gamma_{1,2}} > 0, \ \alpha < 90° \tag{13}$$

where $\gamma_{1,2}$ is the interface energy between the manipulated fluid and the bulk liquid (Figure 12). This means that if we intend to manipulate fluid-2 in the bulk fluid-1, the contact angle between the fluid-2 and the bead should be smaller than 90°.
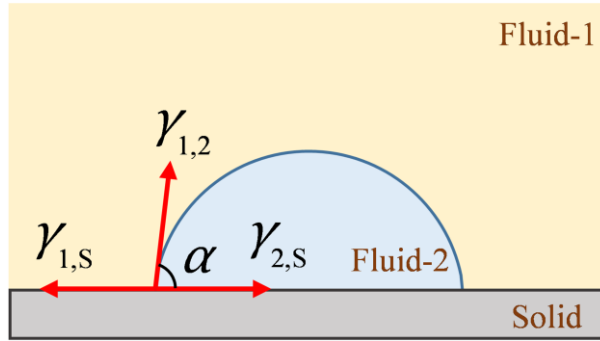
Figure 12. Illustration of the contact angle of fluid 2 in the environment of fluid 1.

Section S5. Analysis of factors influencing the volume of daughter drops

The splitting of the droplet is realized by the breakage of the liquid bridge behind the beads. There are two stages in this process that determine the volume of the daughter-drop. As shown in Figure 13, the first stage is the retraction of the front TCL, which is indicated by the dotted black line. The greater retraction of the front TCL, the smaller the volume of the daughter-drop. The second stage is the retraction of the lateral TCL (the dotted red line). The greater retraction of the lateral TCL, the smaller the volume of the daughter-drop. Therefore, the factors affecting the retraction of the TCLs will show influence on the volume of the daughter-drop.
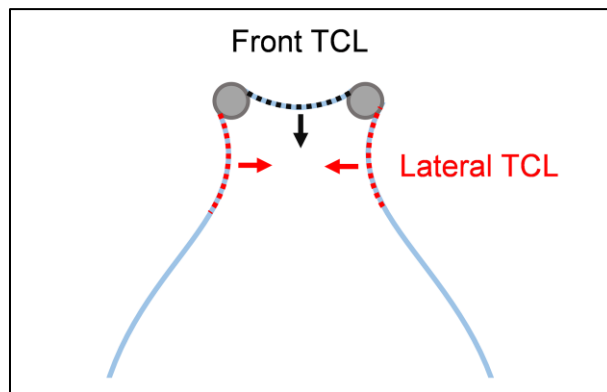

Figure 13. Illustration of the droplet split process

Several factors, including the distance between the beads (D), the size of the beads (d), the liquid surface tension (γ), and the adhesion force between the droplet and the substrate, have an effect on the daughter-drop volume. The experimental results and the analysis as elaborated below:

1. Effect of the distance between the beads (D).

To study the effect of the distance between the beads (D) on the volume of the daughter-drop, we conducted droplet splitting tests with different distances (D) and measured the volumes of the generated daughter-drops (V_d). The measurement of the daughter-drop volume is being briefly described as follows. After splitting, the daughter-drop is drained with a filter paper, and the weight increase of the filter paper is measured with a precision balance. This procedure completes in several seconds, so the water evaporation is ignored. The volume of the daughter-drop is calculated by the weight increase of the filter paper. As shown in Figure 14 and 15, the volume of the daughter-drop increases with the enlarging of the distance between the beads.
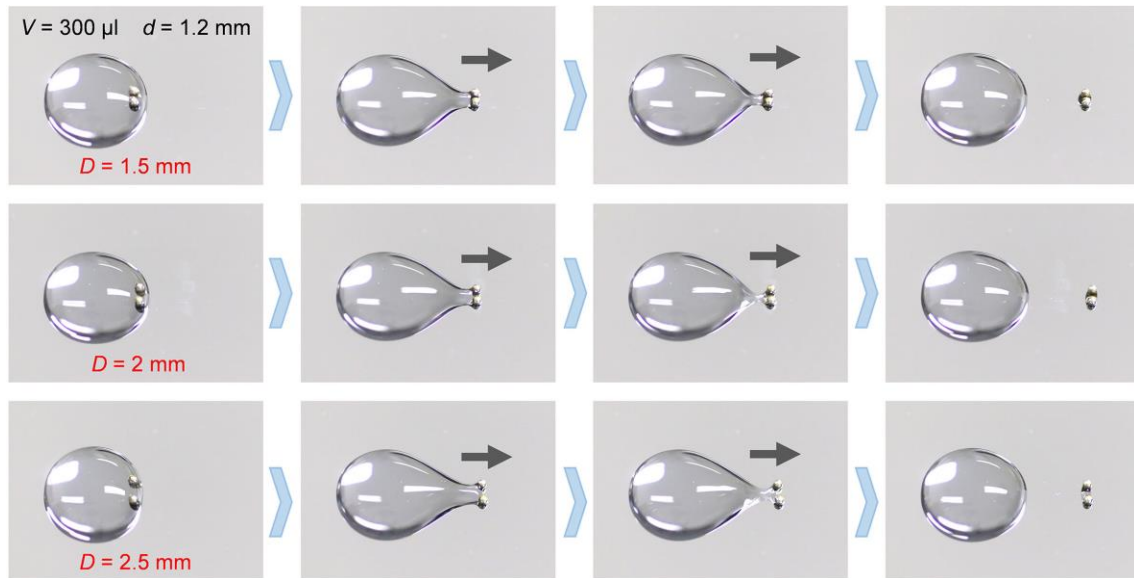

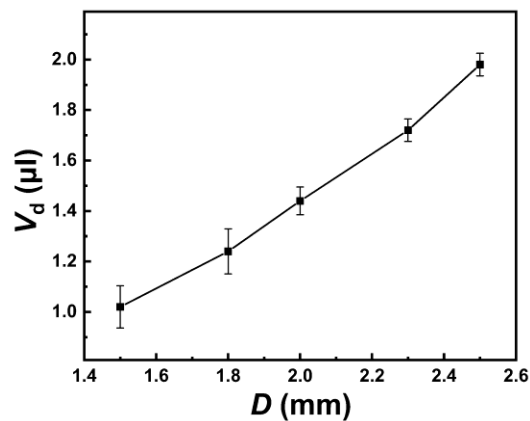**Figure 14. Droplet splitting tests at different distance between the beads (D).**

Figure 15. Dependence the daughter-drop volume on the distance between the beads.

This can be explained from two aspects. On the one hand, according to the analysis in Supplementary Text S1, the relationship between the adhesion at the front TCL (f_{front}) and the distance between the beads (D) can be expressed as

$$f_{\text{front}} = \gamma \cos \theta_{\text{adv}} \cdot (D - d \cos \alpha) \tag{14}$$

Enlarging the distance will increase the f_{front}, which increases the retractions of the front TCL and reduces the volume of the daughter-drop.

On the other hand, the width of the liquid bridge behind the beads (L_2) is positively related with the distance between the beads (D)

$$L_2 = D + d \cos \eta \tag{15}$$

widening the liquid bridge causes the beads to take more liquid away when the liquid bridge raptures. The latter effect is more dominate to the volume of the daughter-drop. Therefore, the volume of the daughter-drop is positively related with the distance between the beads (D).

2. Effect of the size of the beads (d).

To study the effect of the beads size (d) on the volume of the daughter-drop, we conducted droplet splitting tests with different beads sizes (d) and measured the volumes of the generated daughter-drops. As shown in Figure 16 and 17, the volume of the daughter-drop increases with the enlarging of the beads. This is because that according to Equation 1 and 2, enlarging the beads results in the decrease of the adhesion at the front TCL and the widening of the liquid bridge. Both the two effects contribute to the enlargement of the daughter-drop. Therefore, the volume of the daughter-drop is positively related with the size of the beads (d).
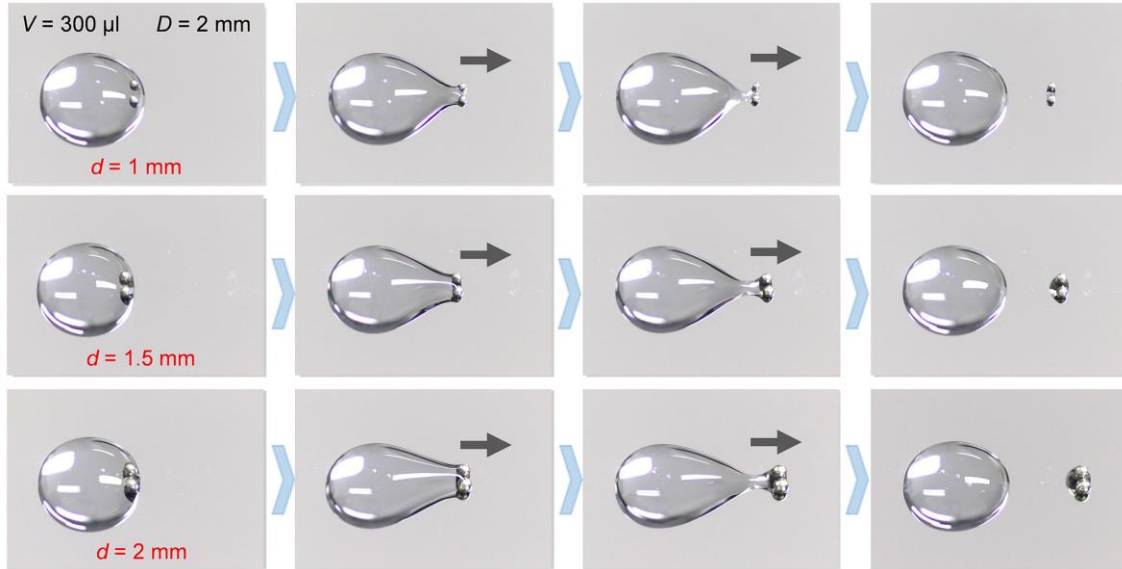
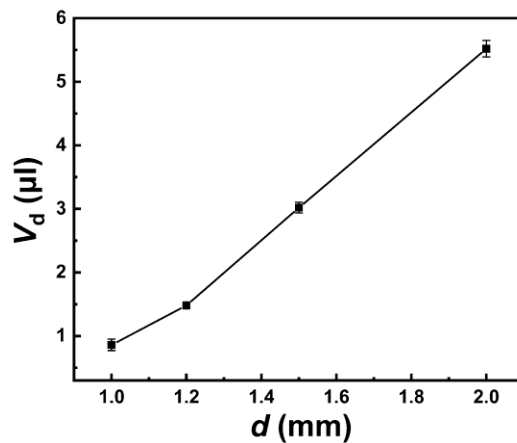**Figure 16. Droplet splitting tests with different sized beads (*d*).**

Figure 17. Dependence of the daughter-drop volume on the bead size.

3. Effect of the volume of the mother droplet (V_o).

To study the effect of the mother droplet volume (V_o) on the volume of the daughter-drop, we conducted droplet splitting tests with different parent droplet volume and measured the volume of the generated daughter-drop. As shown in Figure 18 and 19, the volume of the mother droplet shows not obvious effect on the volume of the daughter-drop. This can be explained that during the generation of the daughter-drop, the retractions of the front and lateral TCLs remain unchanged at different sized mother droplets. Therefore, the volume of the mother droplet shows little influence on the volume of the daughter-drop.
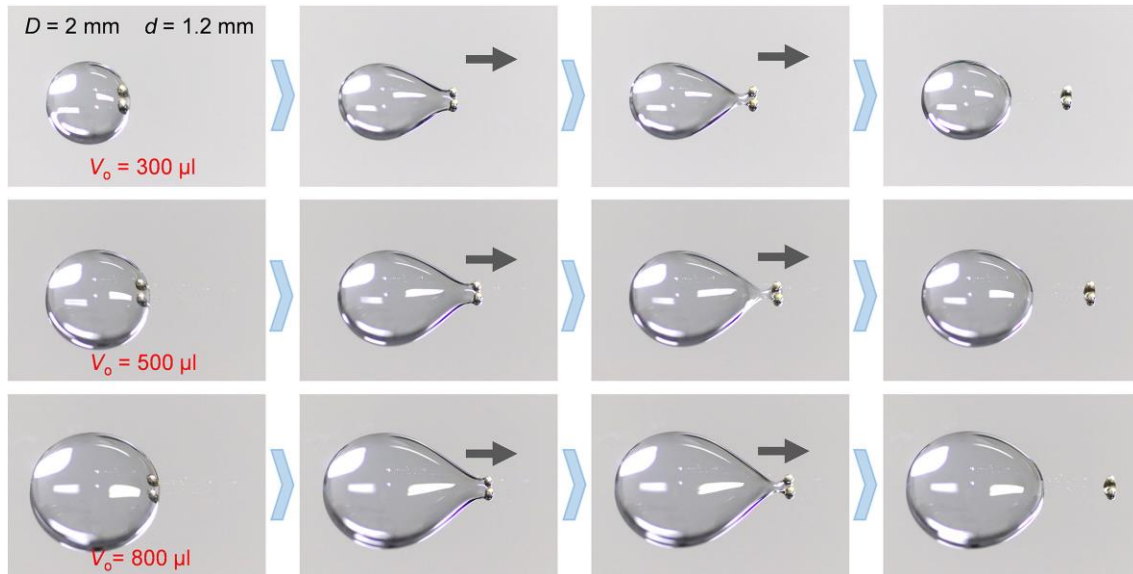
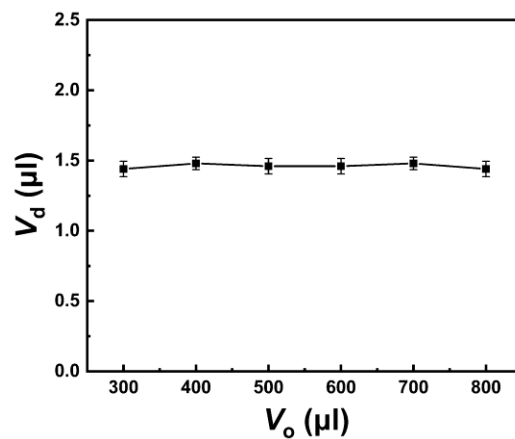**Figure 18. Droplet splitting tests using mother droplet with different volume.**

Figure 19. Dependence of the daughter-drop volume on the mother droplet volume.

4. Effect of the liquid surface tension (γ).

To study the effect of the liquid surface tension (γ) on the volume of the daughter-drop, we conducted droplet splitting tests using droplets with different surface tension (γ), and measured the volume of the generated daughter-drop. As shown in Figure 20 and 21, the volume of the daughter-drop is negatively related with the liquid surface tension. This can be explained that the generation of the daughter-drop results from the rapture of the liquid bridge behind the beads. The smaller of the liquid surface tension, the more difficult of the liquid bridge rapture. As a result, the mother droplet with the smallest surface tension generates the largest daughter-drop.

Indeed, the viscosity of the liquids also varies for different liquids. However, here we only focus on the effect of the surface tension on the volume of the daughter-drop.
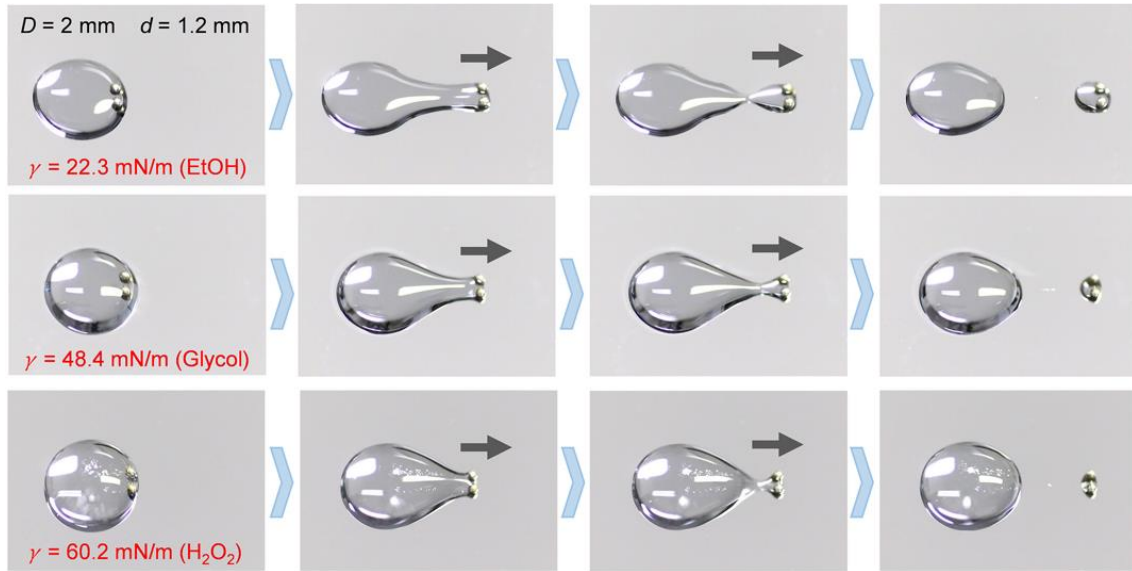

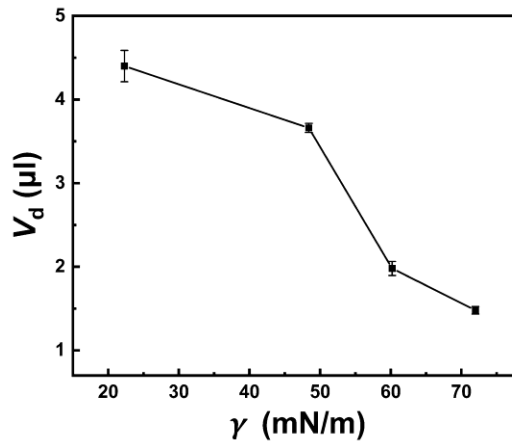**Figure 20. Droplet splitting tests using droplets with different surface tensions.**

Figure 21. Dependence of the daughter-drop volume on the liquid surface tension.

5. Effect of the adhesion force between the droplet and the substrate.

To study the effect of the adhesion force between the droplet and the substrate on the volume of the daughter-drop, we conducted droplet splitting tests on different substrates and measured the volumes of the generated daughter-drops. Here, we used the receding contact angle (θ_{rec}) to indicate the adhesion force between the droplet and the substrate: the substrate has a large adhesion force to the droplet if the droplet has a small receding contact angle on the substrate. As shown in Figure 22 and 23, the volume of the daughter-drop is positively related with the receding contact angles. This is because that the generation of the daughter-drop results from the

retractions of the front and lateral TCLs, and the lateral TCL is more dominant. The retraction of the lateral TCL is determined by the adhesion force (receding contact angles) between the droplet and the substrate. The lateral TCL retracts more easily on a low-adhesive (large receding contact angle) substrate, generating a smaller daughter-drop.
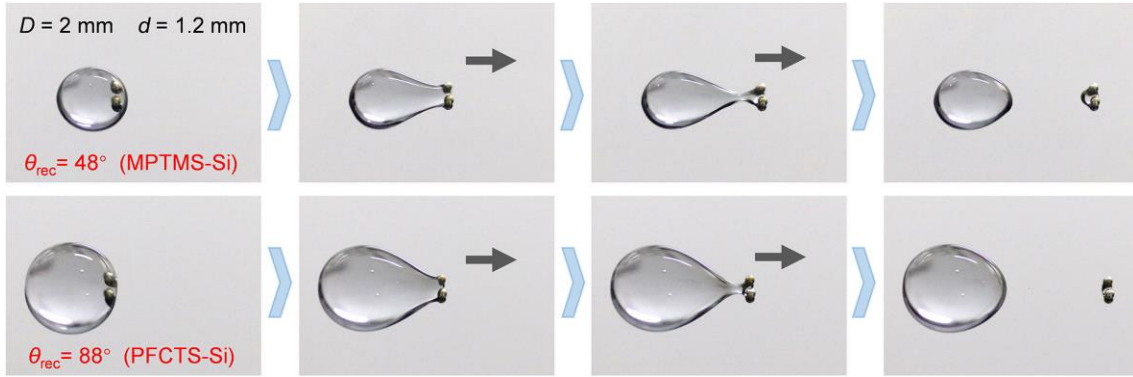

Figure 22. Droplet splitting tests at substrates with different receding angles.
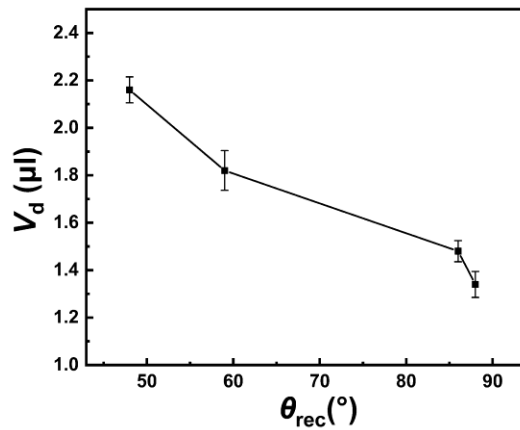

Figure 23. Dependence of the daughter-drop volume on receding contact angle.

We also discuss the number of daughter-drop could be created by single droplet. According to the phase diagram shown in Fig. 2A, reducing the droplet volume leads to the droplet behavior transformation from split to transport. The volume of the mother droplet is set as V_{o}, and the volume of the droplet that can be transported by the robot is set as V_{t}. The number of the daughter-drops n is determined by the volume reduction

$$n = \frac{V_{\mathrm{o}} - V_{\mathrm{t}}}{V_{\mathrm{d}}} \tag{9}$$

where V_d is the volume of the daughter-drop. Accordingly, we use mother droplets with different volumes to for verification. The volume of the daughter-drop is measured to be 1.5 μL, and the volume of the droplet that can be transported is 220 μL. The comparison of the experimental results with the calculated data is shown in Table R3. We can find that the experimental results fit well with the calculated values.

Table R3. Number of daughter-drop (n) split from droplets with different volume.

Droplet volume (μL)	n_1	n_2	n_3	calculated value
230	6	5	6	6
235	10	8	10	10
240	12	13	12	13
245	14	16	15	17
250	18	19	18	20

Section S6. Quantitative evaluation of the mixing efficiency

To quantify the liquid mixing efficiency by the robot rotation, we split a daughter-droplet from a dyed-droplet, and transport it to mix with a pure water droplet. $T = 0$ s is set as the time when the daughter droplet contacts with the pure water droplet, while the time when the pure water droplet is visually homogeneous after contact with the daughter droplet is set as the time of mixing complete. The sequential images in Figure 24 show the comparison of the split, transport, and mix processes at different rotational speeds of 0 revolutions per minute (rpm) and 20 rpm. It takes 11 min and 47 s to complete the mixing process without rotation (0 rpm), compared with a much shorter time of 6 min and 51 s with a rotational speed of 20 rpm.

Moreover, the dependence of the mixing efficiency on the rotational speed is summarized in Table R4. The time required for the mixing completion reduces with the accelerating of the rotation, meaning the mixing efficiency increases with the enlarging of the rotational speed.
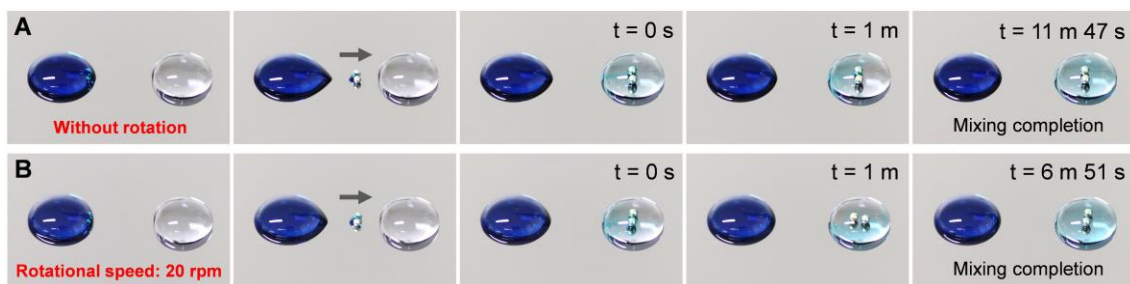
Figure 24. Comparison of droplet mixing with and without rotation.

Table R4. Mixing complete time and mixing efficiency at different Rotational speed.

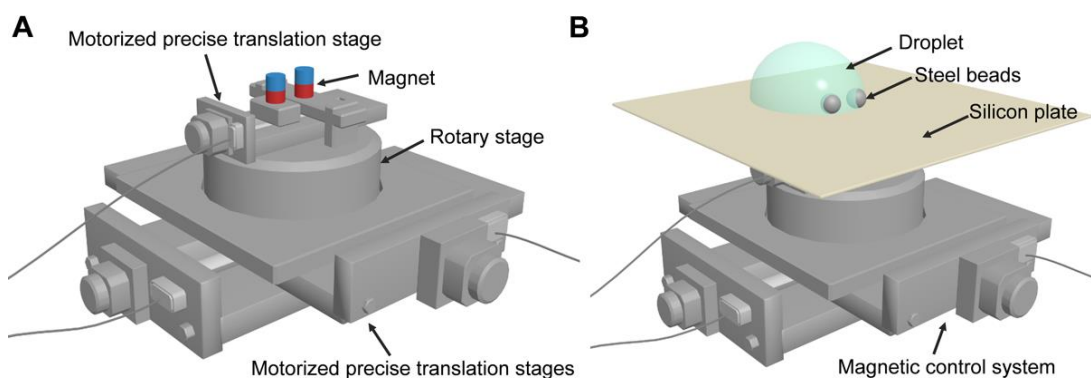| Rotational speed	Mix complete time	Mixing efficiency
0	11m 47s	100%
15 rpm	7m 23s	138%
20 rpm	6m 51s	172%
30 rpm	6m 23s	185%
50 rpm	5m 18s	222%

Fig. S1. Scheme of the magnetic-actuated robot. (**A**) Scheme of the magnetic control system. (**B**) Overview of the droplet manipulation using the magnetic-actuated robot.
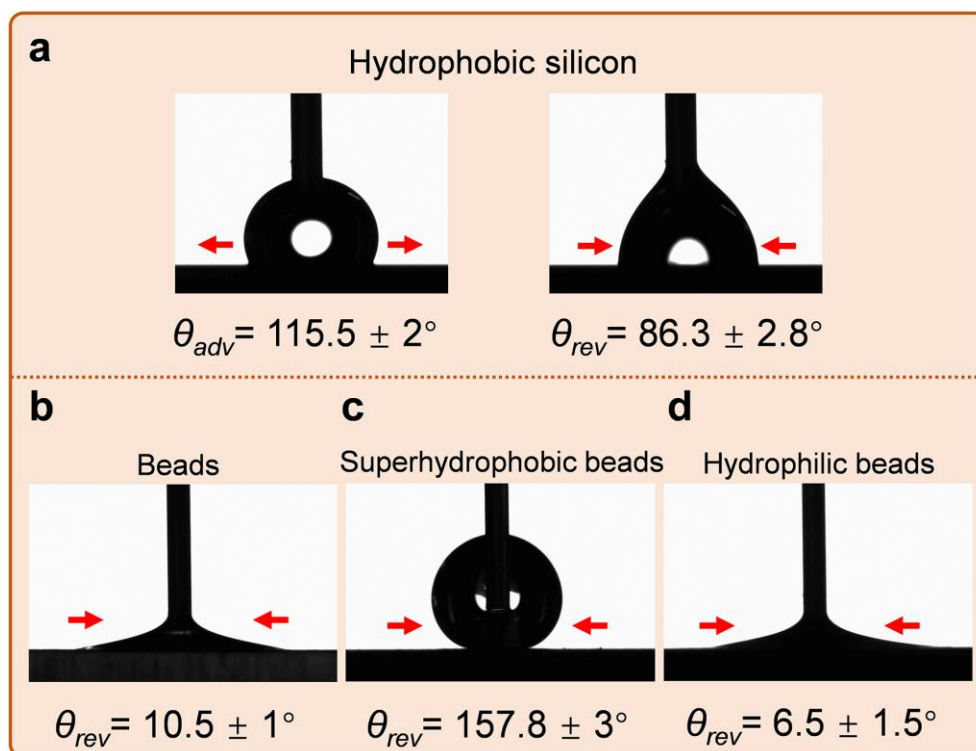
Fig. S2. Contact angle characterization. (**A**) Advancing (θ_{adv}) and receding (θ_{rec}) contact angles of the hydrophobic silicon wafer. (**B**) Receding contact angle of the steel bead. Note that steel plates are used for the contact angles characterization. (**C**) Receding contact angle of the superhydrophobic steel bead. (**D**) Receding contact angle of the superhydrophilic steel bead.
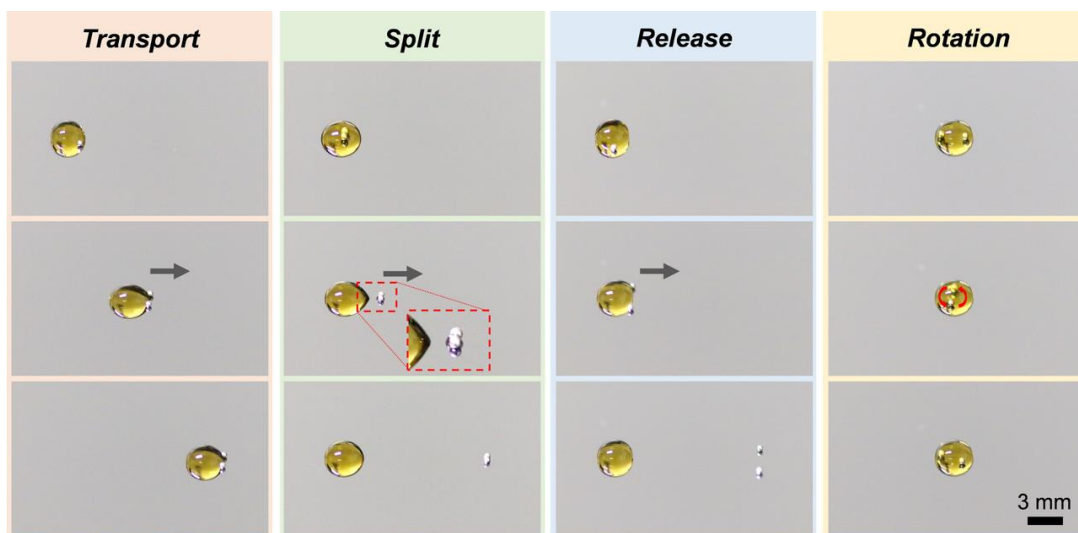
Fig. S3. Micro-droplet manipulation. Microdrops with volume of 9 μl can be transport, split, released and rotated using the robot. The center-to-center distance between the beads are controlled as 2 mm, 0.5 mm, 3 mm, and 2 mm, respectively. The moving speed is 2mm/s.

Fig. S4. Demonstration of the droplet behaviors influenced by *D/d* and *V*. (**A**) Manipulation of droplets by the magnetic-actuated with *D/d* of 1.67. The robot transports a 150 μl droplet to a 200 μl droplet. Then, a daughter-drop is split from the mixing droplet. (**B**) Manipulation of droplets by the magnetic-actuated robot with *D/d* of 3.33. The robot releases the mixing droplet after transport a 150 μl droplet to a 200 μl droplet. The black arrows indicate the moving directions of the robot. The moving speed is 2mm/s. Scale bar, 10 mm.
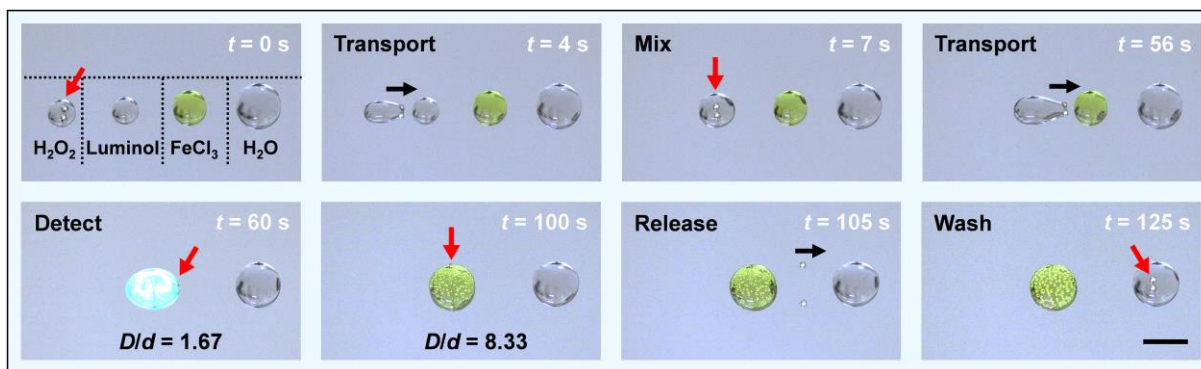
Fig. S5. Demonstration of the luminol reaction. H_2O_2, Luminol, $FeCl_3$, and H_2O droplets are placed on the substrate. The robot transports the H_2O_2 droplet to the Luminol droplet and drive the mixed droplet to the $FeCl_3$ droplet for the detection of Fe^{3+}. Then the robot alters their structure to release the droplet and move to the water droplet for washing and recycling. The volume of H_2O_2 droplet and Luminol droplet is 50 μl. The volume of $FeCl_3$ droplet and H_2O droplet is 150 μl and 250 μl, respectively. The black arrows represent the moving direction of the robot, and the red arrows indicate the position of the beads. The moving speed is 2 mm/s. Scale bars, 10 mm.
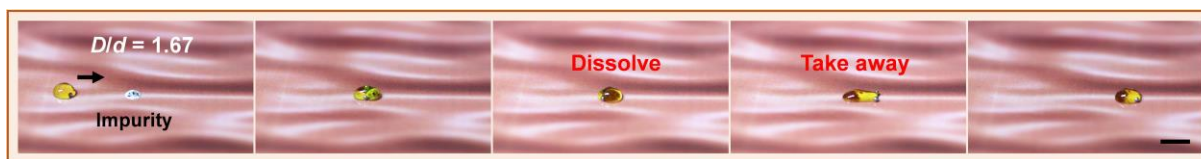
Fig. S6. Demonstrations of the drug delivery using the magnetic-actuated robot. The robot transports a drug droplet to a tumor. After 3 minutes, the tumor is dissolved and taken away from the surface. The black arrows indicate the moving directions of the robots. The moving speed is 2 mm/s. Scale bar, 5 mm.

Movie S1. Typical behaviors of the droplets manipulated using the magnetic-actuated robot.
Water droplets colored with different edible dyes are manipulated using the robot, including capture, transport, split, release, and rotate. The volume of the droplets is 250 μl. The moving speed of the robot is 2 mm/s.

Movie S2. Demonstration of the droplet behaviors influenced by *D/d* and *V*. In the first part, a 150 μl water droplet is transported by the robot, while a daughter-drop is split and moved when enlarging the droplet volume to 350 μl. *D/d* of the robot is 1.67. In the second part, the 350 μl droplet is released by the robot, although the smaller droplet (150 μl) can still be transported. *D/d* of the robot is 3.33. The moving speed of the robot is 2 mm/s.

Movie S3. Generality demonstration of the magnetic-actuated robot. Part 1, oil droplets manipulation under water. The oil droplets (100 μl) are CCl_4 dissolved with Br_2 (left) and styrene (right), respectively. The robot transports the left droplet to mix with the right one. The black arrow indicates the movement of the droplet. Part 2, water droplets manipulation under oil (n-heptadecane). The droplets (50 μl) are water dissolved with KSCN (left) and $FeCl_3$ (right), respectively. The left droplet is captured by the robot and transported to the right one. Part 3, gas bubbles manipulation under water. A superhydrophobic robot can successively collect the gas bubbles (20 μl). The white dotted line indicates the trajectory of the robot. Part 4, manipulation of a water droplet moving up and down on upright surface. The volume of the water droplet is 20 μl. Part 5, manipulation of a water droplet inside a tube. A droplet (20 μl) is actuated by the robot to capture the impurity inside a tube. After 1 minute, the impurity is dissolved and taken away by the droplet. In the experiments above, the moving speeds of the droplet robots are 2 mm/s.

Movie S4. Display of the stepwise acid-based neutralization reactions. In the first step, the robot split a daughter-drop from a NaOH droplet and transport it to a phenolphthalein droplet, which is a commonly used acid-base indicator. In the second step, the robot leaves the indicator droplet, split a 1.5 μl daughter-drop from the HCl droplet, and then move back to the indicator droplet. The volume of NaOH droplet, indicator droplet, and HCl droplet is 250 μl. *D/d* of the robot is 1.67. The moving speed is 2 mm/s.

Movie S5. Display of the luminol reaction. Firstly, the magnetic-actuated robot transports a H_2O_2 droplet to a Luminol droplet. Then the robot drives the mixed droplet to a $FeCl_3$ droplet. After that, the robot enlarges *D/d* from 1.67 to 8.33 to release the droplet. Finally, the robot

moves to a water droplet for washing and recycling. The volume of H_2O_2 droplet and Luminol droplet is 50 μl. The volume of $FeCl_3$ droplet and H_2O droplet is 150 μl and 250 μl, respectively. The moving speed of the robot is 2 mm/s.

Movie S6. Simulation of the calculi removal. The robot transports a droplet of drug to calculi that place on the substrate. The calculi are collected and taken away from the substrate. The volume of the droplet is 20 μl. The moving speed is 2 mm/s.

Movie S7. Simulation of the drug delivery. The robot transports a droplet to the tumor. After 3 minutes, the tumor is dissolved in the droplet. At last, the tumor is taken away from the surface. The volume of the droplet is 20 μl. The moving speed is 2 mm/s.

Movie S8. Simulation of the vascular clearance. The drug droplet and the plaque place inside a tube filled with water. The drug droplet is transported to the plaque by the robot. After 1 minute, the plaque is dissolved and taken away. The volume of the droplet is 5 μl. The moving speed is 2 mm/s.